ADVANCED MATERIALS
www.advmat.de

Synergizing a Large Ordinary Nernst Effect and Axis-Dependent Conduction Polarity in Flat Band KMgBi Crystals

*Andrew M. Ochs, Gerhard H. Fecher, Bin He, Walter Schnelle, Claudia Felser, Joseph P. Heremans, and Joshua E. Goldberger**

The exploration of quantum materials in which an applied thermo/electrical/magnetic field along one crystallographic direction produces an anisotropic response has led to unique functionalities. Along these lines, KMgBi is a layered, narrow gap semiconductor near a critical state between multiple Dirac phases due to the presence of a flat band near the Fermi level. The valence band is highly anisotropic with minimal cross-plane dispersion, which, in combination with an isotropic conduction band, enables axis-dependent conduction polarity. Thermopower and Hall measurements indicate dominant p-type conduction along the cross-plane direction, and n-type conduction along the in-plane direction, leading to a significant zero-field transverse thermoelectric response when the heat flux is at an angle to the principal crystallographic directions. Additionally, a large Ordinary Nernst effect (ONE) is observed with an applied field. It arises from the ambipolar term in the Nernst effect, whereby the Lorentz force on electrons and holes makes them drift in opposite directions so that the resulting Nernst voltage becomes a function of the difference between their partial thermopowers, greatly enhancing the ONE. It is proven that axis-dependent polarity can synergistically enhance the ONE, in addition to leading to a zero-field transverse thermoelectric performance.

1. Introduction

There has been considerable interest in different families of materials that exhibit exotic and complex and anisotropic thermal/electrical/magneto transport phenomena in crystalline materials. This includes the presence of the chiral and thermal chiral anomalies in Weyl semimetals leading to a large nonsaturating magnetoresistance,[1] as well as the presence of large anomalous transverse Nernst Effect ($S_{xy(z)}$) where a temperature gradient along the *x*-direction combined with a magnetic field along the *z*-direction, gives an observed electric field along the *y*-direction) in magnetic materials with large Berry curvatures.[2] A third example is axis-dependent conduction polarity, in which a noncubic compound will simultaneously exhibit either *p*- or *n*-type conduction, depending on the direction of travel.[3] Considering that almost all electronic devices require the integration of separate *p*- and *n*-type materials to direct charge flow and induce functionality, goniopolarity can lead to new device technologies. In recent years, there have been significant efforts elucidating the band structure origins of this phenomenon,[4] expanding the library of compounds that exhibit this effect,[3b] and showing its relevance in applications including transverse thermoelectric and Peltier devices.[3a,5]

A. M. Ochs, J. E. Goldberger
Department of Chemistry and Biochemistry
The Ohio State University
Columbus, OH 43210, USA
E-mail: goldberger@chemistry.ohio-state.edu
G. H. Fecher, B. He, W. Schnelle, C. Felser, J. E. Goldberger
Max-Planck Institute for the Chemical Physics of Solids
01187 Dresden, Germany

J. P. Heremans
Department of Mechanical and Aerospace Engineering
The Ohio State University
Columbus, OH 43210, USA
J. P. Heremans
Department of Physics
The Ohio State University
Columbus, OH 43210, USA
J. P. Heremans, J. E. Goldberger
Department of Materials Science and Engineering
The Ohio State University
Columbus, OH 43210, USA

The ORCID identification number(s) for the author(s) of this article can be found under https://doi.org/10.1002/adma.202308151

DOI: 10.1002/adma.202308151

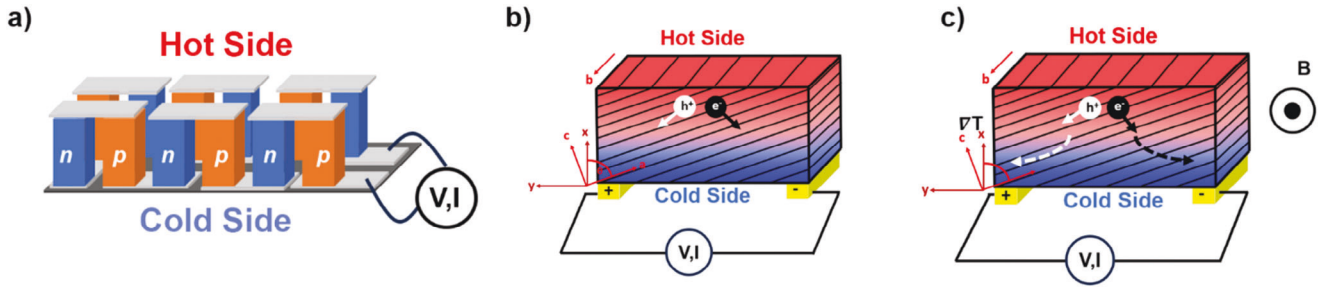

Figure 1. a) Diagram of standard longitudinal thermoelectric generator. b) Diagram of transverse thermoelectric device that utilizes axis-dependent conduction polarity. c) Diagram of transverse thermoelectric device that utilizes axis-dependent conduction polarity augmented by the ambipolar contribution to the Ordinary Nernst effect. In (b,c), the device is constructed from a hypothetical tetragonal layered compound where the cross-plane direction corresponds to the *c*-axis.

This axis-dependent conduction polarity occurs when a material has different band curvatures along different crystallographic directions. It can arise from two possible mechanisms: the single-carrier or multicarrier mechanisms. In the single carrier mechanism, the transport anisotropy is a result of the Fermi level cutting through a single band having opposite curvatures along different directions,[4] and is found in $NaSn_2As_2$,[3c] $PdCoO_2$,[6] and $PtCoO_2$.[6a] In the multicarrier mechanism, the carriers that give rise to *p*-type conduction and *n*-type conduction are in different bands, such that one band is predominant in transport along one direction, while the second band dominates transport along a different direction. This occurs on both metals and semiconductors including Mg, Zn, and Cd,[7] $PdSe_2$,[8] NaSnAs,[3b] Re_4Si_7,[5b] WSi_2,[9] $CsBi_4Te_6$,[10] and $ZrTe_3$.[11]

KMgBi is one material that upon simple inspection of its band structure, is likely to exhibit axis-dependent conduction polarity. This layered, tetragonal material is normally a semiconductor with a narrow bandgap of $E_g = 0.02$ eV, but exists in a critical state and can be tuned to induce a type-I, type-II, or type-III Dirac fermion.[12] This results from the valence band being highly anisotropic with a large dispersion along the in-plane direction, and flat along the cross-plane direction. In contrast, the conduction band is much more isotropic with a relatively large dispersion along both the in-plane and cross-plane directions. Thus, cross-plane conduction is expected to be *n*-type as measured by the Hall or thermopower, while in-plane conduction is likely to have both e^- and h^+ contribute. The overall in-plane conduction polarity will depend on the differences between the hole and electron in-plane effective masses, as well as the relative carrier densities which depend on the presence of extrinsic dopants.

Materials that exhibit axis-dependent conduction polarity has led to the development of efficient transverse thermoelectric and Peltier devices.[5a,b] In these transverse thermoelectric modules, a temperature gradient along one direction of a crystal (x) is converted into voltage gradient along a perpendicular direction (y), thereby eliminating the need for the hot side contacts that exist in conventional longitudinal devices and are subject to degradation (**Figure 1a**).[3a,13] Furthermore, materials that exhibit axis conduction polarity via a two-carrier mechanism are also expected to have a large ordinary Nernst effect, providing both carriers have sufficiently high mobilities[14] potentially enabling further enhancements of transverse thermoelectric efficiency upon application of a magnetic field along a perpendicular direction (Figure 1c). Along these lines, the possibility of axis-dependent conduction polarity in KMgBi as well as the presence of both carrier types in this extremely narrow bandgap semiconductor, makes it an intriguing material for exploring the synergistic combination of Nernst and axis-dependent conduction polarity to maximize transverse thermoelectric responses.

The Nernst thermopower of two-carrier systems with electrons (index *e*) and holes (index *h*) at low magnetic fields (i.e., when the product of mobility and magnetic field is smaller than unity, and the Nernst thermopower is linear in field) consists of the sum of the partial Nernst thermopowers $S_{xy,e}$ and $S_{xy,h}$ of the two carriers as well as a third, ambipolar term ($S_{xx,e} - S_{xx,h}$) that involves the difference between their partial longitudinal thermopowers.[15] The three terms are weighted by the partial electrical conductivities $\sigma_{xx,e}$ and $\sigma_{xx,h}$ and mobilities $\mu_{xx,e}$ and $\mu_{xx,h}$ of the carriers along the direction of the temperature gradient following the formula[15]

$$S_{xy} = \left[S_{xy,e}\sigma_{xx,e} + S_{xy,h}\sigma_{xx,h} + B\left(S_{xx,e} - S_{xx,h}\right)\left(\mu_{xx,e} - \mu_{xx,h}\right)\frac{\sigma_{xx,e}\,\sigma_{xx,h}}{\sigma_{xx,e} + \sigma_{xx,h}}\right] \frac{1}{\sigma_{xx,e} + \sigma_{xx,h}} \quad (1)$$

while the partial Nernst thermopowers $S_{xy,e}$ and $S_{xy,h}$ are each only of the order of 1 μV K^{-1} at 1 Tesla, the partial thermopowers $S_{xx,e}$ and $S_{xx,h}$ are of the order of a hundred μV K^{-1} and the mobilities of electrons and holes in this material are high and different from each other. As a consequence, the third, ambipolar, term, dominates the first two, and becomes surprisingly large. Thus, the application of a magnetic field in high mobility materials with axis-dependent conduction polarity can dramatically alter and enhance transverse thermoelectric transport.

Here, we establish computationally and experimentally the presence of axis dependent conduction polarity in KMgBi. Through the growth of multiple crystals and characterization of the in-plane and cross-plane thermal/electrical/magneto conduction properties from 80 to 300 K, we show negative Seebeck and Hall coefficients along the cross-plane direction indicating dominant *n*-type conduction and positive values along the in-plane direction, indicating dominant *p*-type conduction. These results agree with computational predictions of these properties. Large Ordinary Nernst thermopowers, comparable in magnitude to longitudinal Seebeck coefficients, and large magnetoresistances

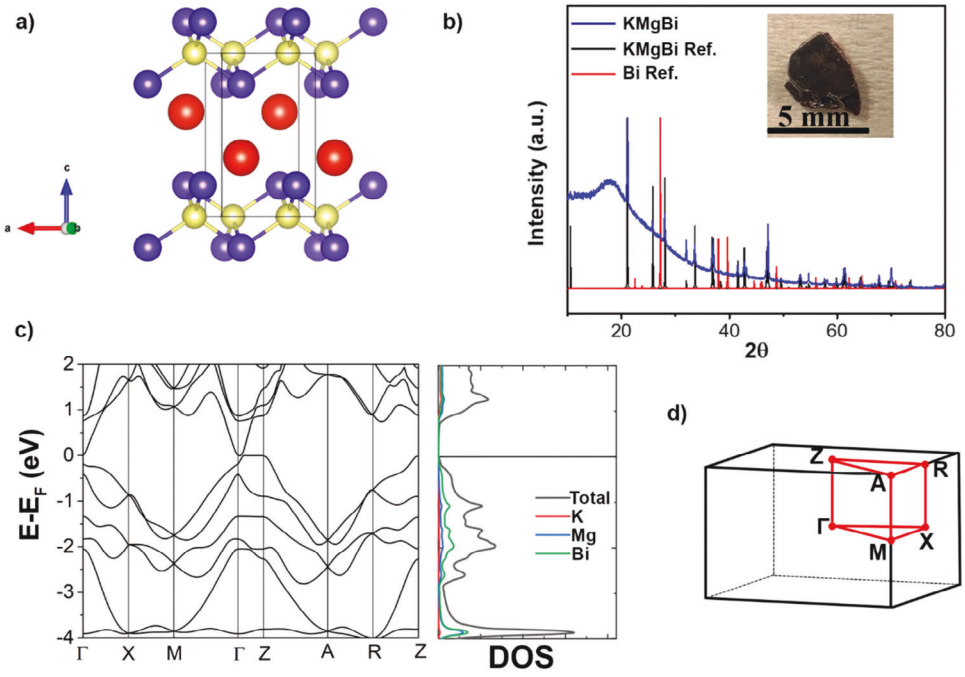

Figure 2. a) Crystal structure of KMgBi (P4/nmm). Yellow spheres represent Mg, purple represents Bi, and red represents K atoms. b) Powder X-ray diffraction pattern of ground KMgBi single crystals. Inset: Photo of a typical KMgBi crystal used for transport measurements. References include KMgBi, and Bi used for flux. c) Calculated band structure (left) and density of states (DOS) of KMgBi. d) Reciprocal space map of the tetragonal Brillouin zone

are observed in both the in-plane and cross-plane orientations, indicating the presence of multicarrier conduction. We estimate from tensor rotations that a 1.4 T magnetic field can increase the transverse thermoelectric figure of merit $z_{xy}T$ from 10% to 300% and from 80 to 300 K. Although the air-sensitivity and overall performance of KMgBi limits its potential applications, this model system establishes how the combination of ONE and axis-dependent conduction polarity can improve the overall performance of transverse thermoelectric devices.

2. Results and Discussion

KMgBi crystallizes into the PbFCl structure-type and has a tetragonal *P4/nmm* space group. This compound features layers of edge-sharing $MgBi_4$ tetrahedra separated by layers of K atoms (**Figure** 2a). In this tetragonal unit cell, the cross-plane direction occurs along the *c*-axis and the in-plane directions occur along the *a*/*b*-axes. Large single crystals were prepared from Bi flux. Figure 2b shows the powder XRD pattern of the ground KMgBi crystals. Due to the high air-sensitivity the XRD pattern was collected under Kapton tape, which has a large background signature at low 2θ, obscuring the relative intensities of peaks. These crystals typically had diameters up to 5 mm and thicknesses of up to 1 mm. These crystal sizes are more than adequate for the measurement of both the in-plane and cross-plane transport properties. Due to the air-sensitivity of KMgBi, all crystals were handled in an N_2-filled glovebox and stored in an evacuated, sealed quartz tube. Air exposure leads to immediate decomposition and degradation. When performing a series of sequential powder XRD experiments of KMgBi encapsulated with a thin Kapton film, over time the KMgBi peaks were observed to decrease in intensity, while new Bi peaks emerged and increased in intensity, as O_2 diffused through the polymer film.

The calculated electronic band structure (Figure 2c,d) further indicates KMgBi have highly anisotropic bands and is consistent with previous angle-resolved photoemission measurements and density functional theory studies.[12] The strong anisotropy of the valence band combined with the isotropic nature of the conduction band give a strong indication that this material will exhibit axis-dependent conduction polarity via a multicarrier mechanism. Near the Fermi level, the valence band is dominated by the Bi $p_{x,y}$ orbitals.[12] Consequently, the valence band is extremely flat along the Γ-Z (cross-plane *c*-axis direction) (Figure 2d) leading to a very large effective mass tensor of holes along this direction. Along the in-plane *a*/*b*-axis directions, the large orbital overlap of the Bi $p_{x,y}$ orbitals in the valence band, leads to a highly dispersion valence band and small effective mass tensor. In contrast, the conduction band has a large dispersion/small effective mass along both the in-plane and cross-plane directions. The states at the bottom of conduction band at Γ belong to the A_{1g} representation, and are delocalized throughout the lattice at the interstitials between the atoms. The PDOS calculations indicate partial contribution from all three elements. Along the cross-plane direction, the large effective mass of the holes and small effective mass of electrons suggests that when both carriers are present, cross-plane transport should be predominantly n-type. In the in-plane directions, both electrons and holes will have similar effective masses and both partially contribute to transport, and thus the dominant carrier type will depend on the fine details of the band structure.

The Seebeck coefficient tensors (S_{aa} and S_{cc}) were calculated from the electronic band structure assuming an isotropic

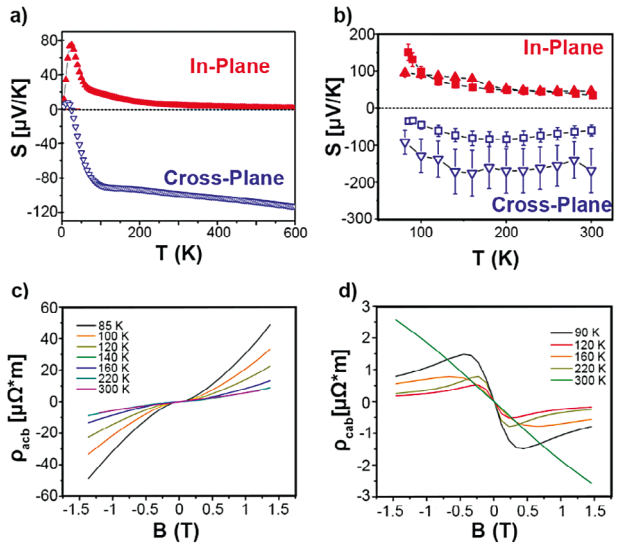

Figure 3. a) Calculated in-plane and cross-plane thermopowers for KMgBi. b) Measured in-plane (red) and cross-plane (blue) thermopowers for KMgBi on two separate single crystals (squares, crystals). c) In-plane Hall resistivities (ρ_{acb}) versus temperature for KMgBi at different temperatures. d) Cross-plane Hall resistivities (ρ_{cab}) versus magnetic field for KMgBi at different temperatures.

scattering time approximation as implemented in the linear Boltzmann equation solver BoltzTraP, and indicate the presence of axis-dependent conduction polarity occurs across a wide temperature range. The in-plane and cross-plane Seebeck coefficients from 5 to 600 K are shown in **Figure** 3a. Across 5–600 K, KmgBi is predicted to have large negative S_{cc} values, and smaller positive S_{aa} values. At 300 K, S_{cc} is −100 μV K^{-1} and small S_{aa} is +7.9 μV K^{-1}. These first principles calculations indicate that S_{aa} decreases with increasing temperature and S_{cc} becomes more negative with increasing temperature. As expected for an anisotropic semiconducting material, the thermopowers along both directions tend to different asymptotes at the high temperature limit on account of the mobility anisotropy. In Figure 3b, the in-plane and cross-plane Seebeck coefficients measured on two separate KmgBi single crystals from 80 to 300 K are shown. Both exhibit positive S_{aa} coefficients that decrease with increasing temperature with values of +39 and +46 μV K^{-1} at 300 K. The S_{cc} coefficients for both crystals are negative, with 300 K values of −170 and −64 μV K^{-1} at 300 K. The differing temperature dependent thermopower coefficients reflect the small differences in doping levels between the two crystals. The measured low-field in-plane (Figure 3c) and cross-plane (Figure 3d) Hall resistivities also have the same signs as the Seebeck coefficients, further confirming dominant hole transport along the in-plane direction and electron transport along the cross-plane direction. Both the in-plane and cross-plane Hall coefficients indicate that there is a larger concentration of holes in the material, compared to electrons. Along the in-plane direction, where hole mobility must be higher than electron mobility, the Hall coefficient remains positive across the entire range of magnetic field strengths. However, along the cross-plane direction, only the low magnetic field portion has a negative coefficient before turning positive at high magnetic field strengths. This is indicative of the presence of a smaller concentration of faster negative carriers that dominating the Hall signal at low-field, before the slower but higher concentration of positive carriers start to dominate at much higher fields. Extracting the relative electron and hole concentrations and anisotropic mobilities using Hall measurements is greatly complicated by the two-carrier nature of this air-sensitive, narrow gap semiconductor, and requires much higher field measurements.

We then measured the thermoelectric transport properties along both the in-plane and cross-plane directions in the absence of magnetic field, and with a magnetic field oriented down the *b*-axis. First, the zero field in-plane (ρ_{aa}) and cross-plane (ρ_{cc}) resistivities are shown in **Figure** 4a, and are 0.152 and 3.84 Ω cm at 300 K, respectively. Along both directions, the temperature coefficients of resistivity change sign at ≈100 K, and indicate semiconducting behavior at low temperature and metallic behavior above this temperature. This transition is expected for narrow-gapped semiconducting materials, and is consistent with previous in-plane transport measurements on KMgBi.[16] The measured in-plane and cross-plane thermal conductivities (κ_{aa} and κ_{cc}, respectively) are given in Figure 4b. The value of κ_{aa} decreases sharply with increasing temperature from 35.4 W m^{-1} K^{-1} at 80 K to 3.40 W m^{-1} K^{-1} at 300 K. κ_{cc} exhibits low values at all temperatures, with a value of 0.929 W m^{-1} K^{-1} at 300 K. Negligible changes in the thermal conductivity (<3%) were observed even 1.4 T field (Figure S2, Supporting Information), and thus Righi–Leduc effects were not investigated. The relatively high electronic resistivities and negligible magnetothermal conductivities both indicate that the thermal conductivity is of predominantly phononic origin. Additionally, an extraordinarily large magneto-Seebeck response is observed along the in-plane direction S_{aab}, for which a 1.4 T field boosts increase the thermopower from 150 to 560 μV K^{-1} (Figure 3c) at 80 K.

A large positive magnetoresistance (MR) of up to 45%, where $\%MR\,(B) = \frac{[\rho(B) - \rho(0)]}{\rho(0)} * 100$, is observed along the in-plane direction (ρ_{aab}) (Figure 4d). A smaller magnetoresistance is observed along the cross-plane direction (ρ_{ccb}, Figure S1, Supporting Information). The in-plane (S_{acb}) and cross-plane (S_{cab}) Nernst thermopowers were measured up to ±1.4 T. A large S_{acb} Nernst thermopower of 150 μV K^{-1} at is observed at 80 K and 1.4 T. The 1 T Nernst thermopowers are on the same order of magnitude as the in-plane and cross-plane Seebeck coefficients (Figure 4e,f) at low temperatures, demonstrating that axis-dependent conduction polarity is a result of a multicarrier mechanism. However, the Nernst thermopower decreases with increasing temperature until it is an order of magnitude smaller than thermopower along both directions at 300 K. This decrease in Nernst with temperature is seen in virtually all materials and is a consequence of decreasing carrier mobility with temperature.[15,17]

While transverse thermoelectric devices that employ either axis-dependent conduction polarity[5a,b] or the ONE[18] have been explored independently, both effects are present in KMgBi, allowing a deeper investigation on the combination of these effects in transverse thermoelectric devices. In transverse thermoelectric devices (Figure 1b,c), the figure of merit ($z_{xy}T$) is conventionally defined as $z_{xy}T = \frac{S_{xy}^2 \sigma_{yy}}{\kappa_{xx}} T$, and the value will change with the application of a magnetic field along *z*. In materials with axis dependent conduction polarity, the largest transverse

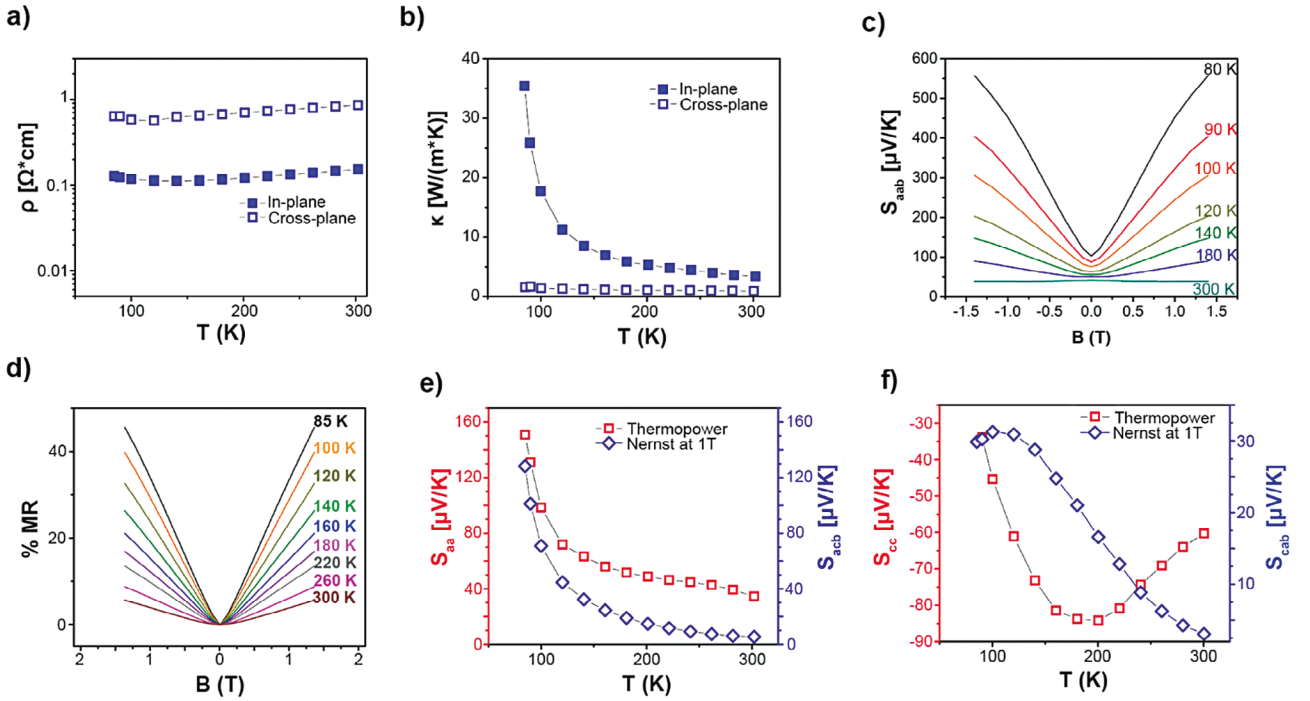

Figure 4. Magneto/thermoelectric transport properties for a representative KMgBi crystal. a) Electrical resistivities along the in-plane (ρ_{aa}, closed squares) and cross-plane (ρ_{cc}, open squares) directions. b) Thermal conductivities measured along the in-plane (κ_{aa}, closed squares) and cross-plane (κ_{cc}, open squares) directions. c) In-plane magnetothermopower S_{aab} measured at different temperatures. d) In-plane percent magnetoresistance versus applied magnetic field at different temperatures. e) In-plane thermopower (S_{aa}) and in-plane Nernst thermopower S_{acb} at 1 T. f) Cross-plane thermopower (S_{cc}) and cross-plane Nernst thermopower (S_{cab}) at 1 T. In all measurements, the magnetic field was applied parallel to the *b*-axis.

thermoelectric effect will occur when the temperature gradient, ∇T_x, and generated electric field, E_y, are rotated away from the orthogonalized directions in the crystal by an angle (θ). For KMgBi, the maximum transverse figure of merit will occur when x and y are rotated away from the in-plane *a*-axis and cross-plane *c*-axis, respectively. To understand how the transverse thermoelectric properties of KMgBi change with rotation angle and applied field, tensor rotations were performed on the measured in-plane and cross-plane thermoelectric properties at each temperature and magnetic field strength keeping the magnetic field vector along the *b*-axis (see the Supporting Information). To emphasize this measurement geometry, we subsequently define the figure of merit as $z_{xy}T = \frac{S_{xzy}^2 \sigma_{zzy}}{\kappa_{xxy}} T$ for the rest of this paper. For comparison, Figure S3 (Supporting Information) shows the tensor extrapolated values of κ_{xx}, S_{xz}, and σ_{zz}, from rotating the direction of the heat gradient (θ) in the absence of a magnetic field. We find that the ideal rotation angle (θ_{max}) that maximizes $z_{xy}T$ varies between 45° and 70° depending on temperature, and magnetic field strength (Figure S4, Supporting Information). At 80 K, θ_{max} varies from 60° to 70° as the applied field changes +1.4 to −1.4 T. At 180 K, θ_{max} varies from 50° to 70° with these same fields, whereas at 300 K, θ_{max} is 55–60° with virtually no field dependence. The changes in θ_{max} with magnetic field indicate that the ONE and magneto-Seebeck effects have a strong contribution to transverse thermopower at low temperatures but have smaller contribution at high temperature.

Finally, we establish how the temperature-dependent transverse thermoelectric properties change upon application of a 1.4 T magnetic field, and at $\theta = 70°$, which are conditions close to where $z_{xy}T$ is maximum (**Figure 5**). At 80 K, the application of a 1.4 T magnetic field dramatically increases S_{xzy} from −45.8 to −198 μV K^{-1}, a factor of ≈ 4.3x. The application of the magnetic field demonstrates how the inherent transverse thermopower from the axis-dependent conduction polarity in KMgBi can be amplified by exploiting the Nernst and magneto-Seebeck effects. In contrast, σ_{zzy} is reduced only by a factor of 1.5x due to magnetoresistance effects. Combined, the application of a +1.4 T field boosts z_{xy}T from 0.024 to 0.35 × 10^{-3}. The application of a −1.4 T field leads to an identical $z_{xy}T$ at $\theta = 125°$ rotation. At the high temperature limit (300 K) when negligible magneto-Seebeck and Nernst effects are present, a magnetic field has a minimal impact on $z_{xy}T$, which has values of ≈0.21 × 10^{-3}. In this temperature regime, the transverse thermoelectric response almost entirely arises from the anisotropic thermopowers from axis-dependent conduction polarity. These trends are also observed at a rotation angle of 45° (Figure S5, Supporting Information). While the overall thermoelectric efficiency is modest (max $z_{xy}T$ of 0.54 × 10^{-3} at 160 K) compared to longitudinal thermoelectric materials or transverse thermoelectrics built almost exclusively using either the ONE effect ($Bi_{0.95}Sb_{0.05}$, $z_{xy}T$ = 0.4 at 180 K, B = 1.2 T),[19] or axis-dependent conduction polarity (Re_4Si_7 $z_{xy}T$ = 0.7 at 980 K),[5a,b] these values are comparable in magnitude to transverse anomalous Nernst devices including $YbMnBi_2$,[2c]

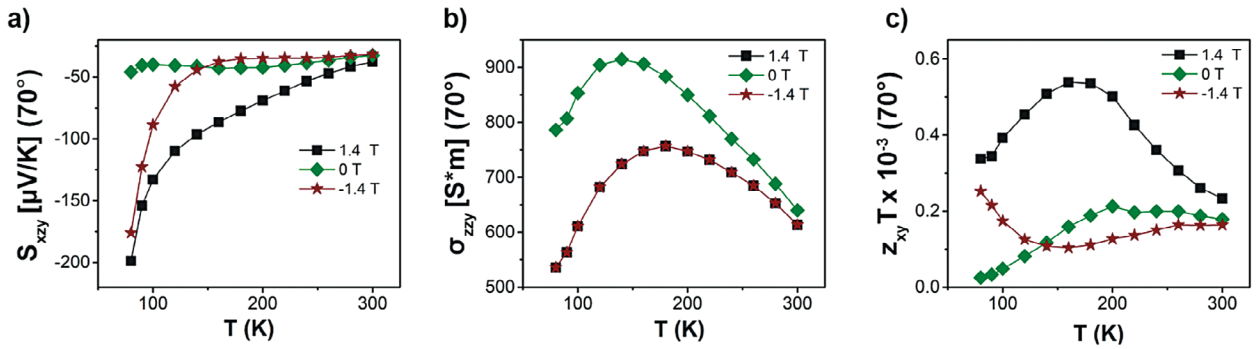

Figure 5. Calculated a) transverse thermopowers, b) electrical conductivities, and c) $z_{xy}T$'s d) from 80 K to 300 K, assuming the thermal gradient is rotated by an angle $\theta = 70°$ away from the *a*-axis along the ac-face, with no magnetic field, and ± 1.4 T magnetic field along the *b*-axis.

and YMn_6Sn_6,[2a] among many other materials[20] which have attracted immense recent interest.

3. Conclusion

The layered, narrow gap semiconductor KMgBi is a unique member in a growing catalog of materials that exhibit axis-dependent conduction polarity. The valence band is highly anisotropic with minimal dispersion along the cross-plane direction, which, in combination with an isotropic conduction band enables axis-dependent conduction polarity in single crystals. Thermopower and Hall measurements indicate dominant *p*-type conduction along the cross-plane direction, and *n*-type conduction along the in-plane direction, leading to a significant zero-field transverse thermoelectric response. In total, the presence of both a large ONE and axis-dependent conduction polarity in KMgBi makes it a model system for understanding experimentally how both effects can combine to enhance the performance of transverse thermoelectric devices. Indeed, at low temperatures, when electron and hole mobilities are sufficiently high, the application of a magnetic field can lead to a significant enhancement in $z_{xy}T$. At high temperatures, the transverse thermoelectric performance is entirely dominated by the anisotropy in themopower, and the application of a magnetic field will have a negligible effect. Overall, this work lays the foundation for transverse thermoelectric generation utilizing both ONE and axis-dependent conduction polarity, and illustrates the intricate balance of a material's anisotropic magneto-thermoelectric, and magneto-electrical conductivities needed to maximize performance.

4. Experimental Section

KMgBi single crystals were synthesized and grown by a Bi flux method. Stoichiometric amounts of K chunks (99.99%, Aldrich), Mg chunks (99.99%, STREM), and Bi shot (99.999%, Alfa Aesar) were added to a alumina Canfield crucible, and additional Bi was added at a 10:1 mass ratio to act as a flux to facilitate crystal growth. The crucible was placed in a quartz ampoule and then sealed at ≈65 mTorr pressure of Ar. The reaction mixture was then heated to 600 °C and held for 3 h, then cooled to 300 °C at a rate of 1.5 °C h^{-1}. At 300 °C, the tubes were quenched, inverted, and rotated in a centrifuge at 1000 rpm for 10 min to separate molten Bi from the KMgBi crystals.

Powder XRD patterns were collected with a Bruker D8 powder diffractometer with Cu Kα radiation from 2θ values from 10° to 80°. Due to the air sensitivity of the crystals, the sample handling and mounting was completed in an N_2-filled glovebox. To prevent decomposition of the crystals, the sample was covered with a layer of Kapton tape. Thermoelectric transport properties were measured using a standard liquid N_2 cryostat at temperatures ranging from 80 to 300 K. A small brass sheet was attached to the top of the crystal underneath a resistance heater, and an alumina sheet acted as a heat sink, assuring uniform heat flow in the samples. Copper-constantan thermocouples were attached at two points along the crystal with Ag epoxy to measure the temperature gradient, and the copper legs of the thermocouples were also used to measure the Seebeck voltage. Thermal conductivity measurements were collected along the in-plane direction using the classical heater-and-sink method, where the amount of heater power divided by the temperature drop across the sample gives the thermal conductance, which is converted to conductivity given the dimensions. Current wires were added to the crystal for the collection of resistivity measurements. For Hall coefficient measurements along the in-plane direction, an additional set of copper wires were attached in a direction transverse to both heat flow and the applied magnetic field, which was varied from −1.4 to +1.4 T. Transport measurements were first performed in the in-plane orientation, then contacts were removed and reattached in the cross-plane orientation, allowing for measurements in both directions to be collected on the same single crystal.

Samples were prepared and transport experiments were performed without ever exposing KMgBi crystals to air. First the electrical contacts were wired inside an N_2-filled glovebox. The cryostat was pumped into the glovebox, upon which the KMgBi crystals were mounted. The cryostat was then sealed, removed, and taken to the measurement set-up. The N_2-filled cryostat was then placed under vacuum, and transport measurements were subsequently performed.

The electronic structure and transport properties of KMgBi was calculated by the full-potential linearized augmented plane-wave (FLAPW) method as implemented in Wien2k[21] in combination with a modified version of Boltztrap,[22] respecting the temperature dependence of the chemical potential.[23] The exchange–correlation functional was taken within the generalized gradient approximation in the Perdew–Burke–Ernzerhof (PBE),[24] parameterization. For integration, a (30×30×30) point mesh was used, resulting in 2176 *k*-points in the irreducible wedge of the Brillouin zone. The energy convergence criterion was set to 10^{-5} Ry and simultaneously the criterion for charge convergence to 10^{-3} e^-. The muffin tin radii were set to $r_{MT} = 2.5a_B$ for all three elements (a_B is Bohr's radius). The r_{MT} values were reduced by 3% during optimization of the lattice parameters and atomic positions using the PBE functional. The position parameters of the structure used for the calculations including spin–orbit interaction are given in Table S1 in the Supporting Information. The lattice parameters of the tetragonal structure with space group P4nmm (129) are: $a = 4.873$ Å and $c = 8.768$ Å. These values are close to those reported from experiments.[25] A comparison of relaxed and experimental crystal structure cannot be performed due to the lack of position parameters from experiment. For the calculation of the transport properties, the tetrahedron method and energy steps of $\approx 0.16 \times 10^{-4}$ Ry were used for integration in Boltztrap. In addition, a quantum theory of atoms

in molecules (QTAIM)[26] analysis of the Bader charges was performed based on the Wien2k calculations using Critic2 (see Table S2 of the Supporting Information).[27]

Supporting Information

Supporting Information is available from the Wiley Online Library or from the author.

Acknowledgements

A.M.O. and J.E.G. acknowledged the Air Force Office of Scientific Research for funding from Grant No. FA9550-21-1-02684. J.P.H. acknowledged the Department of Energy for funding under Grant No. DE-SC0020923, "Discovery of goniopolar metals with zero-field Hall and Nernst effects." J.E.G. also acknowledged the Alexander von Humboldt Foundation for partial support. Partial funding for shared facilities used in this research was provided by the Center for Emergent Materials: an NSF MRSEC under Award No. DMR-2011876. C.F. and B.H. acknowledged Deutsche Forschungsgemeinschaft (DFG, German Research Foundation)-Projektnummer (No. 392228380) and ERC Advanced Grant No. (742068) "TOP-MAT" for funding.

Conflict of Interest

The authors declare no conflict of interest.

Data Availability Statement

The data that support the findings of this study are available from the corresponding author upon reasonable request.

Keywords

axis-dependent conduction polarity, flat band, Nernst effect, topology, transverse thermoelectrics

Received: August 11, 2023
Revised: October 10, 2023
Published online: November 29, 2023

[1] a) C. Shekhar, A. K. Nayak, Y. Sun, M. Schmidt, M. Nicklas, I. Leermakers, U. Zeitler, Y. Skourski, J. Wosnitza, Z. Liu, Y. Chen, W. Schnelle, H. Borrmann, Y. Grin, C. Felser, B. Yan, *Nat. Phys.* **2015**, *11*, 645; b) D. Vu, W. Zhang, C. Sahin, M. E. Flatté, N. Trivedi, J. P. Heremans, *Nat. Mater.* **2021**, *20*, 1525.

[2] a) S. Roychowdhury, A. M. Ochs, S. N. Guin, K. Samanta, J. Noky, C. Shekhar, M. G. Vergniory, J. E. Goldberger, C. Felser, *Adv. Mater.* **2022**, *34*, 2201350; b) B. He, C. Sahin, S. R. Boona, B. C. Sales, Y. Pan, C. Felser, M. E. Flatté, J. P. Heremans, *Joule* **2021**, *17*, 3057; c) Y. Pan, C. Le, B. He, S. J. Watzman, M. Yao, J. Gooth, J. P. Heremans, Y. Sun, C. Felser, *Nat. Mater.* **2022**, *21*, 203; d) W. Zhou, K. Yamamoto, A. Miura, R. Iguchi, Y. Miura, K.-I. Uchida, Y. Sakuraba, *Nat. Mater.* **2021**, *20*, 463.

[3] a) Y. Tang, B. Cui, C. Zhou, M. Grayson, *J. Electron. Mater.* **2015**, *44*, 2095; b) A. M. Ochs, P. Gorai, Y. Wang, M. R. Scudder, K. Koster, C. E. Moore, V. Stevanovic, J. P. Heremans, W. Windl, E. S. Toberer, J. E. Goldberger, *Chem. Mater.* **2021**, *33*, 946; c) B. He, Y. Wang, M. Q. Arguilla, N. D. Cultrara, M. R. Scudder, J. E. Goldberger, W. Windl, J. P. Heremans, *Nat. Mater.* **2019**, *18*, 568.

[4] Y. Wang, K. G. Koster, A. M. Ochs, M. R. Scudder, J. P. Heremans, W. Windl, J. E. Goldberger, *J. Am. Chem. Soc.* **2020**, *142*, 2812.

[5] a) M. R. Scudder, K. G. Koster, J. P. Heremans, J. E. Goldberger, *Appl. Phys. Rev.* **2022**, *9*, 021420; b) M. R. Scudder, B. He, Y. Wang, A. Rai, D. G. Cahill, W. Windl, J. P. Heremans, J. E. Goldberger, *Energy Environ. Sci.* **2020**, *14*, 4009; c) M. Omprakash, H. Usui, K. Yanagi, Y. Mizuguchi, Y. Goto, *Mater. Today Commun.* **2022**, *31*, 103558.

[6] a) K. P. Ong, D. J. Singh, P. Wu, *Phys. Rev. B* **2010**, *104*, 176601; b) P. Yordanov, W. Sigle, P. Kaya, M. E. Gruner, R. Pentcheva, B. Keimer, H.-U. Habermeier, *Phys. Rev. Mater.* **2019**, *3*, 085403.

[7] V. A. Rowe, P. A. Schroeder, *J. Phys. Chem. Solids* **1970**, *31*, 1.

[8] R. A. Nelson, Z. Deng, A. M. Ochs, K. G. Koster, C. T. Irvine, J. P. Heremans, W. Windl, J. E. Goldberger, *Mater. Horiz.* **2023**, *10*, 3740.

[9] K. G. Koster, Z. Deng, C. E. Moore, J. P. Heremans, W. Windl, J. E. Goldberger, *Chem. Mater.* **2023**, *35*, 4228.

[10] D.-Y. Chung, T. P. Hogan, M. Rocci-Lane, P. Brazis, J. R. Ireland, C. R. Kannewurf, M. Bastea, C. Uher, M. G. Kanatzidis, *J. Am. Chem. Soc.* **2004**, *126*, 6414.

[11] C. Felser, E. W. Finckh, H. Kleinke, F. Rocker, W. Tremel, *J. Mater. Chem.* **1998**, *8*, 1787.

[12] D. F. Liu, L. Y. Wei, C. C. Le, H. Y. Wang, X. Zhang, N. Kumar, C. Shekhar, N. B. M. Schröter, Y. W. Li, D. Pei, L. X. Xu, P. Dudin, T. K. Kim, C. Cacho, J. Fujii, I. Vobornik, M. X. Wang, L. X. Yang, Z. K. Liu, Y. F. Guo, J. P. Hu, C. Felser, S. S. P. Parkin, Y. L. Chen, *J. Appl. Phys.* **2021**, *129*, 235109.

[13] a) M. Hamid Elsheikh, D. A. Shnawah, M. F. M. Sabri, S. B. M. Said, M. Haji Hassan, M. B. Ali Bashir, M. Mohamad, *Renewable Sustainable Energy Rev.* **2014**, *30*, 337; b) H. J. Goldsmid, *J. Electron. Mater.* **2011**, *40*, 1254.

[14] K. Behnia, H. Aubin, *Rep. Prog. Phys.* **2016**, *79*, 046502.

[15] E. H. Putley, *The Hall Effect and Related Phenomena*, Butterworth & Co., London **1960**.

[16] X. Zhang, S. Sun, H. Lei, *Phys. Rev. B* **2017**, *95*, 035209.

[17] K. Behnia, *J. Phys.: Condens. Matter* **2009**, *21*, 113101.

[18] M. Murata, K. Nagase, K. Aoyama, A. Yamamoto, Y. Sakuraba, *iScience* **2021**, *24*, 101967.

[19] P. Jandl, U. Birkholz, *J. Appl. Phys.* **1994**, *76*, 7351.

[20] a) S. Isogami, K. Masuda, Y. Miura, N. Rajamanickam, Y. Sakuraba, *Appl. Phys. Lett.* **2021**, *118*, 092407; b) K.-I. Uchida, W. Zhou, Y. Sakuraba, *Appl. Phys. Lett.* **2021**, *118*, 140504; c) J. Wang, Y.-C. Lau, W. Zhou, T. Seki, Y. Sakuraba, T. Kubota, K. Ito, K. Takanashi, *Adv. Electron. Mater.* **2022**, *8*, 2101380.

[21] a) P. Blaha, K. Schwarz, G. K. Madsen, D. Kvasnicka, J. Luitz, *Wien2k. An Augmented Plane Wave+ Local Orbitals Program for Calculating Crystal Properties*, (Ed: K. Schwarz), Vienna University of Technology, Vienna, Austria, **2023**; b) P. Blaha, K. Schwarz, P. Sorantin, S. B. Trickey, *Comput. Phys. Commun.* **1990**, *59*, 399; c) K. Schwarz, P. Blaha, *Comput. Mater. Sci.* **2003**, *28*, 259.

[22] a) G. K. H. Madsen, D. J. Singh, *Comput. Phys. Commun.* **2006**, *175*, 67; b) T. Graf, G. Fecher, J. Barth, J. Winterlik, C. Felser, *J. Phys. D: Appl. Phys* **2009**, *42*, 084003; c) S. Ouardi, G. H. Fecher, B. Balke, X. Kozina, G. Stryganyuk, C. Felser, S. Lowitzer, D. Ködderitzsch, H. Ebert, E. Ikenaga, *Phys. Rev. B* **2010**, *82*, 085108.

[23] J. Nayak, G. H. Fecher, S. Ouardi, C. Shekhar, C. Tusche, S. Ueda, E. Ikenaga, C. Felser, *Phys. Rev. B* **2018**, *98*, 075206.

[24] J. P. Perdew, K. Burke, M. Ernzerhof, *Phys. Rev. Lett.* **1996**, *77*, 3865.

[25] R. Vogel, H.-U. Schuster, *Z. Naturforsch., B* **1979**, *34*, 1719.

[26] R. F. W. Bader, *Atoms in Molecules: A Quantum Theory*, Oxford University Press, Oxford **1990**.

[27] a) A. Otero-De-La-Roza, M. A. Blanco, A. M. Pendás, V. Luaña, *Comput. Phys. Commun.* **2009**, *180*, 157; b) A. Otero-De-La-Roza, E. R. Johnson, V. Luaña, *Comput. Phys. Commun.* **2014**, *185*, 1007.